A Computational Study of Preferential Diffusion and Scalar Transport in Nonpremixed Hydrogen-Air Flames

Jieyu Jiang [a], Xi Jiang [b *], Min Zhu [c]

[a] State Key Laboratory of Fire Science, University of Science and Technology of China, Hefei, Anhui 230026, China

[b] Engineering Department, Lancaster University, Lancaster LA1 4YR, United Kingdom

[c] Department of Thermal Engineering, Tsinghua University, Beijing 100084, China

Abstract

The nonpremixed hydrogen-air reacting flow is simulated using three-dimensional direct numerical simulation coupled with flamelet generated manifolds based on detailed chemical kinetics. From the comparisons between one computational case taking into account preferential diffusion and another case with unity Lewis number assumption, the instantaneous results show that the flow is more vortical in the absence of preferential diffusion. This indicates that preferential diffusion may smooth the flame under certain circumstances when coupled with the intrinsic hydrodynamic instability. The flame compositional structures are also influenced by preferential diffusion in a significant manner. Further, the statistical information suggests that turbulent scalar flux is affected by preferential diffusion. The phenomenon of counter-gradient diffusion of both the conserved and non-conserved scalars can be detected for the two cases. The gradient model for scalar closure is found to be incapable of accurately predicting the scalar transport in nonpremixed hydrogen flames.

Key Words: Nonpremixed hydrogen flames, direct numerical simulation, preferential diffusion, turbulent scalar transport, counter-gradient diffusion

1. Introduction

Emissions of pollutants from the combustion of conventional fossil fuels in energy utilization applications have caused major environmental concerns and the massive CO_2 emissions have been regarded as an important contributor to global climate change [1]. There is no doubt that clean energy solutions such as hydrogen-enriched fuels may play an increasingly important role in future energy supply. Hydrogen with a very large mass diffusivity and low molecular weight is a very promising energy carrier. The benefits of hydrogen call for further studies of the combustion of H_2, in particular, for the development of an advanced model for simulating turbulent nonpremixed flames such as jet flames of hydrogen or hydrogen-enriched fuels in future low emission combustion devices and engines.

Because hydrogen is highly diffusive, it may have impacts not only on the chemical process but also on the stability of flame. The phenomenon associated with the fact that each species has a different mass diffusion velocity in a multi-species flow system, is referred to as differential diffusion. According to Graham's law [2], the diffusion rate of a gas is inversely proportional to the square root of its molecular weight, which can be stated as $\frac{D_1}{D_2} = \sqrt{\frac{W_2}{W_1}}$. Therefore, hydrogen molecules diffuse four times faster than those of oxygen. Differential diffusion exists in multi-species flows. When considering the combustion heat, the mass diffusivity of hydrogen is much faster than the thermal diffusivity. This is attributed to

preferential diffusion, which is usually discussed in the flow considering combustion. An important parameter in characterizing preferential diffusion effects is the Lewis number *Le*, defined as the ratio of thermal diffusivity to mass diffusivity.

In many earlier studies, single one-step chemistry and unity Lewis number assumptions were used in the computational studies but they were not able to accurately predict the combustion process [3-5]. In the last few decades, there have been an increasing number of studies investigating preferential diffusion, including studies using laminar flamelet approach reported by Pitsch and Peters [6], Nilsen and Kosály [7], while experimental investigations [8-10] were also carried out. It was verified that the preferential diffusion effects in the premixed bluff body flames initially increased with Reynolds number, and then saturated and persisted at higher Reynolds numbers. In addition, the influences of preferential diffusion on the maximum flame temperature and burning rate were investigated using two-dimensional direct numerical simulations (DNS) [11, 12], where the details of turbulence and vortex shedding were missing. Preferential diffusion could result in a shift in the equivalence ratio to leaner conditions and was sensitive to different compositions of fuel [13-16]. Furthermore, the probability density function mixing models [17, 18], the effective Lewis numbers [19] and the conserved mixture fraction models [20, 21] were developed and applied for preferential diffusion in computational studies. Since the differences between preferential diffusion and homogeneous effects are strong in such flames, a predictive model cannot be developed without understanding of the effects of preferential species transport on turbulent nonpremixed flames.

In the context of either large eddy simulation or Reynolds averaged Navier-Stokes

approach, it is necessary to provide closure modeling for turbulent scalar flux terms. The gradient hypothesis is often used in the turbulent scalar transport in conjunction with turbulent eddy viscosity concepts for premixed flames [22, 23]. If *c* represents a composition variable, according to the gradient transport hypothesis, the corresponding turbulent scalar transport $\widetilde{u''c''}$ in the *i*th direction is modeled as

$$\bar{\rho}\widetilde{u_i''c''} = -\bar{\rho}D_t \partial\tilde{c}/\partial x_i \tag{1}$$

Here ρ is the density and the overbar represents the Reynolds averaged operation, and D_t is the turbulent eddy diffusivity. For a general quantity *q*, Favre averaged quantity $\tilde{q}$ is defined as $\tilde{q} \equiv \overline{\rho q}/\bar{\rho}$ and $\tilde{q} = q - q''$. Under some conditions the gradient hypothesis fails to predict either the magnitude or the direction of turbulent scalar transport, and indeed the existence of counter-gradient diffusion (CGD) in premixed flames has been detected from experimental data [24, 25], theoretical analysis and numerical simulations [26–31]. CGD refers to the phenomenon of turbulent scalar fluxes moving in the same direction as the local mean gradient of the scalar, in violation of the conventional but most widely used gradient diffusion (GD) model. This was found in the early analyses of Bray [32] for premixed flames. Later, advanced closures for the turbulent flux terms were proposed by Veynante et al. [33] and Zimont et al. [34]. It has been found the occurrence of CGD is closely related to the pressure distribution across the flame brush due to the heat release, and the gradient model fails to accurately predict the scalar transport of turbulent premixed flames. Robin et al. [35] proposed an extended closure of the reactive scalar fluxes with one contribution that involved the flame wrinkling factor, and the corresponding closure has been then successfully applied to impinging flames [36]. The premixed flame is developed when oxidizer has been mixed

well with fuel, which can create a thin flame front as all of the reactants are readily available. However, nonpremixed flame is mainly controlled by the fuel/oxidizer mixing and diffusion with combustion mainly taking place in the shear layer of the jet flame. Since the conditions corresponding to nonpremixed and premixed combustion mechanisms are somehow different, could the gradient model be available for predicting the turbulent scalar transport in nonpremixed flames? It has been discussed in the early study by Luo and Bray [37] in supersonic diffusion flames, and has been verified in the experimental investigation of Caldeira Pires and Heitor [38]. CGD is found to be related to the importance of the heat release in the vicinity of stoichiometric conditions which affects the normalized specific volume variations, as recently emphasized by Serra et al. [39]. Although advanced closures are generally proposed for the premixed turbulent flames, there is still a lack of detailed investigations on the closure modeling for nonpremixed flames.

This study was aimed to investigate the effects of preferential diffusion on nonpremixed hydrogen flames, and more importantly, to evaluate the gradient model of turbulent transport using fully three-dimensional (3D) DNS results based on detailed chemistry mechanism and transport. Two simulations have been carried out, with one simulation based on the realistic preferential diffusion and the other one based on the unity Lewis number assumption. The rest of the paper is organised into four sections: governing equations and chemistry mechanism are given in section 2, flame configuration and numerical approach are presented in section 3, results and discussion are described in section 4 and conclusions are briefly summarised in section 5.

2. Governing Equations and Chemistry Mechanism

In this study, the nonpremixed hydrogen-air reacting flow is considered as an unsteady compressible viscous fluid with buoyancy effects and chemical reactions. Three-dimensional governing equations for the reacting flow field, including mass conservation, momentum transfer, energy conservation, and transport equations for progress variable and mixture fraction, are solved in their non-dimensional form:

$$\frac{\partial \rho}{\partial t} = -\frac{\partial (\rho \mathbf{u}_j)}{\partial x_j}, \tag{2}$$

$$\frac{\partial (\rho \mathbf{u}_j)}{\partial t} = -\frac{\partial (\rho \mathbf{u}_j \mathbf{u}_k)}{\partial x_k} - \frac{\partial p}{\partial x_j} + \frac{1}{\mathrm{Re}} \frac{\partial \tau_{jk}}{\partial x_k} - (\rho_a - \rho) \frac{g_j}{Fr}, \tag{3}$$

$$\begin{aligned} \frac{\partial \rho e}{\partial t} = & -\frac{\partial (\rho e \mathbf{u}_k)}{\partial x_k} - \frac{\partial (p \mathbf{u}_k)}{\partial x_k} + \frac{1}{\mathrm{Re}\,\mathrm{Pr}\, M^2 (\gamma - 1)} \frac{\partial \mathbf{q}_k}{\partial x_k} \\ & + \frac{1}{\mathrm{Re}} \frac{\partial (\mathbf{u}_j \tau_{jk})}{\partial x_k} - (\rho_a - \rho) \frac{g_k \mathbf{u}_k}{Fr}, \end{aligned} \tag{4}$$

$$\frac{\partial (\rho Y)}{\partial t} = -\frac{\partial (\rho \mathbf{u}_k Y)}{\partial x_k} + \frac{1}{\mathrm{Re}\,\mathrm{Pr}} \frac{\partial}{\partial x_k} (\rho D_Y \frac{\partial Y}{\partial x_k}) + \omega_Y, \tag{5}$$

$$\frac{\partial (\rho Z)}{\partial t} = -\frac{\partial (\rho \mathbf{u}_k Z)}{\partial x_k} + \frac{1}{\mathrm{Re}\,\mathrm{Pr}} \frac{\partial}{\partial x_k} (\rho D_Z \frac{\partial Z}{\partial x_k}), \tag{6}$$

Equation of state:

$$p = \frac{\rho T}{\gamma M^2} \tag{7}$$

Here t, u_j, e, p stand for time, velocity components in the x_j direction, total energy per unit mass, and pressure respectively. With reference to properties in the fuel stream at the inflow including the jet nozzle diameter l_0, fuel velocity u_0 and the ambient temperature T_0, the non-dimensional form of the governing equations was derived and reported previously

[40]. In addition, the transport and thermal coefficients λ, C_P, μ, γ, W_Y which are calculated and stored in the flamelet generated manifolds (FGM) data table, represent heat conductivity, specific heat at constant pressure, dynamic viscosity, ratio of specific heats, source term of the progress variable. The non-dimensional numbers *M, Pr, Fr, Re* represent Mach number, Prandtl number, Froude number, and Reynolds number respectively [40].

In considering flame chemistry and transport in computationally demanding numerical simulations of multi-species reacting flow systems, many reduction techniques were developed using chemistry only and not taking the transport process into account. In this study, the FGM table for a stoichiometric hydrogen/air mixture [40, 41] was computed using detailed chemical kinetics transport processes as a function of mixture fraction and progress variable. The detailed reaction mechanism includes 7 species and 7 reversible reactions. Two FGM databases are required to be constructed in the present study. One database is generated with unity Lewis number assumption and another is constructed with preferential diffusion. The manifolds have been parameterized by two control variables: the mixture fraction *Z* and the progress variable *Y*. In this study, the mass fraction of H_2O is selected as the progress variable. Flamelets are computed with a detailed reaction mechanism and transport models including preferential diffusion and homogeneous effects respectively. The solutions for manifold flamelets are stored in a lookup table for H_2-Air system, based on counter-flow nonpremixed flamelets [40]. The nonpremixed manifolds, which result from the flamelet calculations, are taken as the input data for the 3D DNS of hydrogen-air reacting flow in the coupling of DNS and FGM. When the two FGM databases are accessed in the DNS solver, bilinear interpolation is used with the local values of mixture fraction and progress variable so

that the values of the dependent variables can be returned.

The transport coefficients are generally defined as complicated functions of temperature and chemical composition of the mixture. However, with unity Lewis number assumption, the diffusion coefficients for Y and Z in the FGM approach are given by $\rho D_Y = \rho D_Z = \frac{\lambda}{C_P}$. Consequently, the transport equations for progress variable for the unity Lewis number assumption in their non-dimensional form can be written as:

$$\frac{\partial(\rho Y)}{\partial t} = -\frac{\partial(\rho \mathbf{u}_k Y)}{\partial x_k} + \frac{1}{\mathrm{Re}\,\mathrm{Pr}}\frac{\partial}{\partial x_k}\left(\frac{\lambda}{C_P}\frac{\partial Y}{\partial x_k}\right) + \omega_Y, \tag{8}$$

To describe the preferential diffusion effects, another equation for the progress variable Y is implemented as a valid alternative to the transport equation Eq. (8). Instead of equation Eq. (8) used in the unity Lewis number case, a new transport equation considering preferential diffusion is derived as [40, 41]

$$\frac{\partial(\rho Y)}{\partial t} = -\frac{\partial(\rho \mathbf{u}_k Y)}{\partial x_k} + \frac{1}{\mathrm{Re}\,\mathrm{Pr}}\frac{\partial}{\partial x_k}\left(\frac{\lambda}{C_p}\frac{\partial Y}{\partial x_k}\right) + \frac{1}{\mathrm{Re}\,Sc_Y}\frac{\partial}{\partial x_k}\left(\rho D_{YZ}\frac{\partial Z}{\partial x_k}\right) + \omega_Y, \tag{9}$$

where ρD_{YZ} is the diffusion coefficient for preferential diffusion calculated by the FGM technique. The diffusivity D_{YZ} is related with the non-unity Lewis number, which has been derived by Swart et al. [42]. It is worth noting that the species diffusion contribution in Eq. (9) can be split in two parts $\frac{\partial}{\partial x_k}\left(\rho D_{YZ}\frac{\partial Z}{\partial x_k}\right)$ and $\frac{\partial}{\partial x_k}\left(\frac{\lambda}{C_P}\frac{\partial Y}{\partial x_k}\right)$, which represent the contributions from preferential diffusion and homogeneous effects respectively. To investigate the preferential diffusion effects on the hydrogen-air nonpremixed flames, the above two equations were respectively considered in the two simulations performed for comparison.

3. Flame Configuration and Numerical Approach

3.1 Flame Configuration

Simulations are performed in a 3D nonpremixed jet flame configuration. The hydrogen fuel jet which is located in the bottom center of the domain is issued into an ambient environment of air from a round nozzle. The initial temperature at the nozzle is subject to a high non-dimensional value of 4.0 (about 1100 K), which is chosen to ensure auto-ignition of the mixture when fuel and air mix with each other. Fig. 1 shows the geometry of the nonpremixed hydrogen-air free jet flame configuration considered here. The computational domain has a size of twelve jet nozzle diameters (12D) in the streamwise direction *x*, transverse direction y and spanwise direction *z* respectively. The present computational domain ($L_x = L_y = L_z = 12$D) has been selected to ensure affordable computational costs for the simulations performed, while the essential flame dynamics is still captured. The governing equations are numerically discretized in a uniform Cartesian grid with 768×768×768 points resulting approximately 452 million nodes. In order to trigger the unstable mode of free jet, the following unsteady velocity perturbation was artificially added to all three inflow velocity components,

$$u' = v' = w' = A\sin\left(2\pi f_0 t\right) \tag{10}$$

where the non-dimensional amplitude of the unsteady disturbance is A = 0.06 and the corresponding frequency is f_0 = 0.3. Reynolds number used is Re = 2,000 based on the inlet reference quantities and Froude number is Fr = 1.0.

3.2 Numerical Schemes

Highly accurate numerical schemes are necessary in DNS because turbulence cannot be

resolved using lower-order numerical schemes where numerical diffusion can be larger than the small-scale turbulent transportation. The spatial first- and second-order derivatives in all three directions are solved using a sixth-order accurate compact finite difference (Padé) scheme [43], which are expressed as:

$$f'_{i-1} + 3 f'_i + f'_{i+1} = \frac{7}{3}\frac{f_{i+1} - f_{i-1}}{\Delta x} + \frac{1}{12}\frac{f_{i+2} - f_{i-2}}{\Delta x} \tag{11}$$

$$f''_{i-1} + \frac{11}{2} f''_i + f''_{i+1} = 6\frac{f_{i+1} - 2 f_i + f_{i-1}}{\Delta x^2} + \frac{3}{8}\frac{f_{i+2} - 2 f_i + f_{i-2}}{\Delta x^2} \tag{12}$$

The Padé scheme is arranged in a way that sixth-order accuracy at the inner points, fourth-order next to the boundary points, and third-order at the boundary are achieved by a compact finite differencing, which is found to be both stable and accurate. Solutions for the spatial discretised equations (11)-(12) are obtained by solving the tridiagonal system of derivatives equations. In addition, the discretised equations are advanced in time using a fully explicit low-storage third-order Runge-Kutta scheme [44]. The time step is limited by the Courant-Friedrichs-Lewy (CFL) condition number for stability and the CFL number is selected as 5 for the reacting flow simulations, where the viscosity increases significantly with temperature. Moreover, an increase in the local product mass fraction of more than 0.01% is not allowed for one time step. The simulation results were tested to be time step independent.

3.3 Boundary Conditions

Boundary conditions applied in the simulations are also illustrated in Fig. 1. The computational domain contains the inflow and outflow boundaries in the streamwise direction. The inflow is specified using the Navier-Stokes characteristic boundary conditions [45] based

on the analysis of characteristics waves with temperature treated as a soft variable, which is calculated during the simulation rather than fixed and allowed to fluctuate according to the characteristic waves at the boundary. Non-reflecting characteristic boundary condition (CBC) is used for the outflow boundary. Because the flow is not necessarily going out of the domain instantaneously in the direction normal to the outflow boundary due to the existence of multidimensional vortical structures [46]. A sponge layer [47] next to the outflow boundary has been set from x= 11.75 to the outflow boundary, and this was used to control the spurious wave reflections from the outside of the computational domain by manipulating the flow in the sponge layer. The solution in the sponge layer was forced to approach the averaged values of the flow variables obtained from an upstream "average zone" where the statistical information has been averaged over a region from x=11.5 to x= 11.75. These methods have been proved to be very effective to control the wave reflections through the outflow boundary. In addition, the nonreflecting CBC is also used at the side boundaries.

4. Results and Discussion

Hydrogen-air nonpremixed jet flames including the interactions emerged from hydrogen-air chemical reaction and combustion heat release, species diffusion and fluid convection involving turbulent mixing, thermal conduction and convection are obtained by 3D DNS coupled with FGM based on detailed chemistry mechanism. In the following sub-section 4.1, instantaneous results of flame structures are described in detail, while sub-section 4.2 contains the statistical data of turbulent scalar transport.

4.1 Local Structure of Nonpremixed Hydrogen Flames

To understand the effect of preferential diffusion on flame structures in realistic combustion process, results from the two simulation cases are presented for comparisons. Fig. 2 shows the flame compositional structures between the case using the unity Lewis number assumption and the other case calculated with the preferential diffusion included. The mass fraction distributions of the two cases are evidently different, where the mass fractions of O_2, H, OH and HO_2 for the unity Lewis number case in Fig. 2 (a1, a2, a3, a4) seem to be more vortical than the results of the other case. This is due to the effects of species diffusion on the flame compositional structures in the combustion process. It is worth pointing out that the corresponding distributions for the case with the preferential diffusion in Fig. 2 (b1, b2, b3, b4) are relatively well organized with smoother flame surfaces. Moreover, this trend has been observed in all the instantaneous results obtained from the simulations of the two cases, although only one sample time instant is shown in Fig. 2 for brevity. The flame compositional structures have been influenced by differential diffusion, which suggests that the local mixing of species and the progress of chemical kinetics are also different. This variation could have an impact on the flame temperature and the structures of flow fields shown subsequently.

The flame dynamics of hydrogen-air free jet can be further appreciated from the distributions of velocity vector fields shown in Fig. 3 for the two cases at three different time instants t = 16 (a1, b1), 20 (a2, b2), 24 (a3, b3). The red line is the centerline of the initial reacting flow, which can be treated as a marker for the variation of flame structure. Both cases exhibit complex behaviours associated with the flow vortical structures and their interaction with flamelets. The outer vortical structures of hydrogen free jet in the two cases are generated mainly because of the buoyancy effects due to the interaction between the density

inhomogeneity and gravity. This instability of flame structure associated with the formation of outer vortex is referred to as the buoyancy instability [40, 48]. The distorted tendency of vortical structures in the unity Lewis number case in Fig. 3 (a1, a2, a3) seems stronger. In both cases, the development of vortical structures is also related to the external disturbance added at the jet nozzle exit. The unsteady velocity disturbance is added to the inflow velocity component, which perturbs the inflexional velocity profile. Consequently, the shear instability associated with inflexional velocity shear is amplified by the unsteady velocity perturbation. This flow instability can interact with buoyancy instability, leading to complex and distorted vortical structures in the reacting flow fields.

Both the buoyancy instability and shear instability can be considered as flow hydrodynamic instabilities. The hydrodynamic instability is responsible for the formation of the squeezed and bulged vortical structures and for the wrinkling observed over the flame surface caused by the variations of density and velocity in the flow field. Apart from the hydrodynamic instability, the diffusive-thermal effect on the flame structure is an important factor leading to combustion instability. It is worth pointing out that two main types of flame instabilities existed in the preferential diffusion case in Fig. 3 (b1, b2, b3), which are the hydrodynamic instability and the preferential diffusive-thermal instability caused by preferential diffusion. As combustion proceeds, a rapid change in temperature and in turn in density and other transport properties of fluid significantly affects the momentum transfer which is the driving force for hydrodynamic instability. In the reacting flow using the unity Lewis number assumption, vortical structures are predominately due to buoyancy and velocity shear instabilities. When considering preferential diffusion, a consequence of diffusive effects

on the nonpremixed flame is obtained. An interesting observation is that the flame structures in the unity Lewis number case display relatively stronger instabilities with more distortion of the vortices, whereas the flame structures in the case considering preferential diffusion show weaker instabilities with less distorted vortices. The vortical structures in Fig. 3 (b1, b2, b3) are distributed around the locations near the central red marker line, compared with a tendency of shifting away from the marker line in the unity Lewis number case shown in Fig. 3 (a1, a2, a3). The flame structures in the absence of preferential diffusion display relatively more distortions of vortical structures. This tendency is attributed to the hydrodynamic instability associated with the wrinkling over flame surface, which is the predominant unstable factor of the flame instabilities when ignoring the effect of differential diffusion. However, the flame structures in the case considering preferential diffusion show a different situation with less distorted vortices, which is attributed to the preferential diffusive-thermal instability induced by preferential transport. This indicates that the preferential diffusive-thermal instability may stabilize the flames when coupled with the hydrodynamic instability for the nonpremixed hydrogen jet flame.

Scatterplots of mass fractions of O_2 (a1, b1), H (a2, b2), OH (a3, b3) and HO_2 (a4, b4) in the mixture fraction space for the two cases are shown in Fig. 4. Peak values of O_2 mass fraction in Fig. 4 (a1, b1) are the same for the two cases corresponding to the ambient air condition (about 0.22), while mass fraction of O_2 decreases sharply at around the stoichiometric condition due to the large consumption of O_2. It can been observed that the distribution of O_2 mass fraction in Fig. 4 (b1) for the case considering preferential diffusion is mainly concentrated in the leaner conditions of mixture fraction (in the range of 0.02 – 0.2),

and the relevant dense distributions of O_2 in Fig. 4 (a1) for unity Lewis number case exist in the mixture fraction range of 0.2 – 0.5. As for the radical H, the same trend can be observed. For the radical OH, the maximum mass fraction is around 0.008 in Fig. 4 (a3) for the unity Lewis number case while it is 0.013 in Fig. 4 (b3) for the case considering preferential diffusion. This is associated with the reaction $H + O_2 \rightarrow O + OH$, which contributes directly to the chain branching process by the production of OH radical, and reaction $HO_2 + H \rightarrow 2OH$, which becomes more significant with an increased concentration of HO_2 and results in the production of two OH radicals from a single H radical and HO_2 intermediate. In Fig. 4, the radical HO_2 in the case considering preferential diffusion is also located primarily in the mixture fraction range of 0.02 – 0.2, similar to that of radical H. The distributions of species concentrations are influenced by preferential diffusion in a significant manner, because each species has a different mass diffusivity.

The high diffusivity of H_2 is attributed to preferential diffusion, which may have an impact on the flame structures. The diffusive effects can make a great contribution to flame temperature distributions, as shown in Fig. 5. According to the temperature distributions plotted in Fig. 5 (a1, b1), the higher values of scattered temperature from $T = 6$ to $T = 9$ selected from the temperature fields are shown in the mixture fraction space. The distribution of scattered temperature in Fig. 5 (b1) is clearly widened for the case considering preferential diffusion with respect to the case using the unity Lewis number assumption. In addition, the corresponding peak value of temperature is higher than that for the unity Lewis number case. Apart from these, the mixture fraction corresponding to the peak of temperature distribution is located at near $Z = 0.03$ for the unity Lewis number case in Fig. 5 (a1), but the location of

corresponding mixture fraction for the case considering preferential diffusion in Fig. 5 (b1) shifts towards the side of lower values. This is consistent with the previous finding that preferential diffusion results in a shift in the mixture fraction to leaner conditions [49, 50].

As seen in Fig. 4, the radical H as a major species of the nonpremixed hydrogen flame, has a large concentration in the present flames. The maximum concentration of radical H is roughly three orders of magnitude larger than that of HO_2. As shown in the scatterplots of each species in the flame compositional structures, major species H_2 and H account for a large proportion in the flame compositional structure, and they are predominant in promoting the propagation of the corresponding elementary reaction. Considering the fact that radical H has a significantly larger diffusivity compared with other species in the present flames, it tends to implicate that H radical is an important factor in the burning process and flame compositional structure. Considering the different transport, the Lewis number of each species *i* is expressed as $Le_i = D_T / D_{Mi}$, where D_T is the thermal diffusivity and D_{Mi} is the mass diffusivity of species *i*. It is noticed that the Lewis numbers of major species H_2 and H are both very small, and the corresponding mass diffusivities for H_2 and H exceed the thermal diffusivity. However, for the unity Lewis number case, the thermal diffusivity is equal to the mass diffusivities of each species, leading to quicker thermal energy dissipation due to the relatively strong thermal diffusivity [51]. As a result, the small Lewis numbers of major species H_2 and H can lead to a positive net energy due to stronger mass diffusion than the energy loss by thermal diffusion. That is the reason that why the flame temperatures in Fig. 5 in preferential diffusion case are higher than those in the unity Lewis number case.

In nonpremixed flames, the scalar dissipation rate is an important representative variable,

which provides a useful local time scale for diffusive transport based on the scalar gradients. To calculate the scalar dissipation rate for nonpremixed combustion, the expression related to mixture fraction $\chi = 2\frac{\lambda}{\rho C_P}\left|\nabla Z\right|^2$ has frequently been used to characterize the mixing time scale in the analysis of DNS results of nonpremixed combustion [52]. This expression reflects the contributions from the intensity of local mixing process $\left|\nabla Z\right|^2$ and the change of heat diffusion $\frac{\lambda}{\rho C_P}$. As seen in Fig. 5 (a2, b2), the scalar dissipation rates for the unity Lewis number case presents higher values than those for the case considering preferential diffusion. The maximum scalar dissipation rate for the unity Lewis number case in Fig. 5 (a2) is about 1500, while that for the case considering preferential diffusion in Fig. 5 (b2) is near 1100. Since the scalar dissipation rate is treated as a useful measurement of the turbulent strain effect in nonpremixed flames, where the turbulent strain acts to increase the scalar gradients, the values of scalar dissipation rate is largely dependent on the gradient of mixture fraction *Z* [53]. Associated with the observation in Fig. 3 (a1, a2, a3), the squeezed and bulged effect is much prominent in the absence of preferential diffusion, which promotes the turbulent strain effect. This tendency could benefit the local mixing process and the variation of density, and then the local mixing intensity $\left|\nabla Z\right|^2$ could be intensified in the absence of preferential diffusion. This implies that the local mixing intensity is much larger in the unity Lewis number case, which is related to the strong turbulent strain effect due to the flame wrinkling. In contrast, the smoother flame surface in Fig. 3 (b1, b2, b3) would lead to the weaker turbulent strain effect, and then the values of scalar dissipation rate and local mixing intensity could decrease. The corresponding turbulent strain effect and the distribution of scalar

dissipation rate are consistent with the distributions of velocity vector fields shown in Fig. 3.

4.2 Turbulent Scalar Transport of Nonpremixed Hydrogen Flames

The aforementioned instantaneous results from DNS can be used to reveal the local flame structures and dynamics, which can also be used to provide statistical information on the reacting flow field. Additional information on the turbulent scalar transport of nonpremixed hydrogen flames are extracted from the statistical data of DNS results by time-averaging the relevant quantity at each point of the reacting flow field. Reynolds or Favre averaging quantities at each point are evaluated from t = 16 to t = 24 (about 20000 statistical data for a single point). This section concentrates on the analysis of scalar transport results obtained from the direct solution of governing equations without any closure models.

As seen in Fig. 6, the variation of density-weighted scalar flux $\widetilde{u''Y''}$ is plotted against the scalar gradient of Favre-averaging reaction progress variable $\partial\tilde{Y}/\partial x$. It is worth noting that the scalar flux of progress variable is calculated by $\widetilde{u''Y''}=\overline{\rho u''Y''}/\bar{\rho}=\overline{\rho(u-\tilde{u})(Y-\tilde{Y})}/\bar{\rho}$, but the modelled scalar flux is closely related to the scalar gradient calculated by $\partial\tilde{Y}/\partial x=\partial(\overline{\rho Y}/\bar{\rho})/\partial x$. The calculated and modelled scalar fluxes display a different distribution between the unity Lewis number case (a) and the case considering preferential diffusion (b). Both the ranges of calculated and modelled scalar fluxes in the case considering preferential diffusion are clearly widened, while narrow distributions are formed in the unity Lewis number case. The main discrepancy between the two cases lies in the diffusion process. The preferential diffusion affects the mixing and combustion heat release. To some extents the turbulent scalar flux is influenced by the preferential diffusion, due to the presence of the highly diffusive H_2 as well as the highly diffusive radical H.

According to the gradient model in Eq. (1), when turbulent scalar flux is in the same direction as the local mean gradient of the scalar, the value of D_t would have to be negative, which renders the gradient model invalid. This phenomenon is referred to as CGD. On the contrary, a kind of GD takes place for turbulent scalar transport. Therefore, CGD can be detected from either the first or the third quadrant, where the scalar flux and scalar gradient are all positive or negative, while GD is shown in the second or the forth quadrant. It can be observed that the phenomenon of CGD in Fig. 6 (a, b) accounts for a large proportion of the scalar transport, indicating that CGD may occur in turbulent scalar transport for nonpremixed flames. For both the unity Lewis number case and for the case considering preferential diffusion, the gradient diffusion model fails completely to describe the scalar flux of progress variable in the nonpremixed hydrogen flames.

The gradient model is found to be incapable of describing the non-conserved scalar flux as shown in Fig. 6. Further to this, the corresponding analysis of conserved scalar flux is illustrated in Fig.7. Averaged quantity of conserved scalar flux $\widetilde{u''Z''}$ is obtained from the statistics of mixture fraction *Z*. It is interesting to note that CGD still occurs in the first and third quadrants as expected, where there is no sign change between the scalar flux $\widetilde{u''Z''}$ and scalar gradient $\partial\tilde{Z}/\partial x$. Therefore, CGD can be detected from both the conserved and non-conserved scalars in nonpremixed flames in the two simulations conducted. The gradient transport model is found to be inappropriate to describe both the conserved and non-conserved scalar flux in the nonpremixed flames whether considering preferential diffusion or not.

In Fig. 7, the dense distributions of CGD are visible in the first quadrant for both cases. It

is noted that the range of non-conserved scalar flux for the case considering preferential diffusion in Fig. 6 (a) is wider than that for the unity Lewis number case in Fig. 6 (b), while this trend of conserved scalar flux is relatively attenuated in Fig. 7. Considering governing equations (5)-(6), the difference between the distributions in Fig. 6 and Fig. 7 may be related to the contribution of the source term, which may lead a wider range for the progress variable distribution. Since the contribution of the source term is not negligible for the solution of non-conserved scalar (reaction progress variable), it may be speculated that the distributions have been affected by this term. Nevertheless, a more detailed analysis is needed before a solid conclusion can be drawn.

In order to identify the region where CGD is present, additional analysis is performed. The streamwise profile of the progress variable flux shown in Fig. 8 is selected at (y = 6, z = 6), which is the geometrical centerline of the flame where the combustion is intense and the heat release effect is predominant downstream of the reacting flow field, while the other streamwise profile of the non-conserved scalar flux plotted in Fig. 9 is obtained from the statistical data at the shear layer (y = 5.5, z = 6), which is near the region where the turbulent motion plays a key role apart from the contribution of mixing and chemical reaction. It is noticed that there is a large area of CGD behavior at the centerline of reacting flow field in the range of x = 2 ~ 5 in Fig. 8. Moreover, the large amount of CGD can be seen not only in the unity Lewis number case in Fig. 8 (a) but also in the case considering preferential diffusion in Fig. 8 (b). The distribution of mass fraction of each species (as shown in Fig. 2) indicates the flame compositional structure. In the reacting flow fields, the fresh gases exist mainly in the region from the jet nozzle exit (inflow boundary of the computational domain) to x = 2, and

the productions of intermediates and final combustion products are distributed extensively in the region above $x = 2$. In fact, the locations from $x = 2$ to $x = 5$ correspond to an important area, it is the interface region between the fresh fuel and burnt gas, where the range of averaged progress variable is distributed widely from 0 to 1. In this region, combustion is intense and the role of heat release is prominent. This is the reason why the scalar gradient in this range presents a large value. The interface area between the unburned hydrogen and burned products is mainly controlled by thermal expansion due to combustion heat release, the variation of temperature and density can be significant. This can lead to a strong pressure gradient in the nonpremixed flame in this region. The pressure gradient could cause forced convection of the vortices, and the flow field is subject to the strong forced convection, which may lead to the occurrence of counter-gradient transport. From this physical viewpoint, the pressure-driven convective transport is closely related to the occurrence of counter-gradient transport, and heat release in the interface region between the burnt gas and unburnt fresh fuel subject to the pressure variation across the turbulent flame plays a primary role in the occurrence of counter-gradient transport. This is consistent with the results for premixed flames [26], where a favorable pressure gradient tends to promote counter-gradient turbulent transport.

In addition, the streamwise profile of non-conserved scalar flux in Fig. 9 provides more details with respect to the major factors leading to CGD. It can be found that the sign of the calculated and modelled fluxes changes frequently and then the large area of CGD behavior ever seen in Fig. 8 disappears. Instead, the local CGD phenomenon still occurs, where the calculated and modelled fluxes keep the same sign. This phenomenon displays a quite

different distribution compared with the region shown in Fig. 8. Combined with the fact that both mixing and turbulent motion are predominant at the shear layer, apart from the contribution of chemical reaction, the local CGD, instead of a large region of CGD, is consequently developed. For both the unity Lewis number case and the case considering preferential diffusion, the local CGD of progress variable can take place, while large regions of CGD concentrate at the center of reacting flow where the strong pressure gradient across the interface area between the unburned hydrogen and burned products could promote the counter-gradient transport, which is mainly controlled by thermal expansion due to combustion heat release. As discussed above, the occurrence of CGD in nonpremixed flame is primarily relevant to the pressure gradient dominated by heat release in the combustion process. The detailed analyses of transport equation and the quantitative budget of pressure term will be discussed systematically in our following study. From the qualitative aspect, it can be concluded that the gradient model is incapable of accurately predicting the scalar transport in nonpremixed hydrogen flames, and a suitable model associated with pressure gradient terms need to be developed for nonpremixed flames in the future, which may account for both the GD and CGD behaviors.

5. Conclusions

In hydrogen-related clean combustion applications, preferential diffusion can affect the flame structure and chemical reaction process and in turn the combustion efficiency and system stability. Results suggest that flame compositional structures including species O_2, H, OH and HO_2 are different when considering preferential diffusion. The vortical structures and

distortions in velocity vector fields for the unity Lewis number case are weakened in the case considering preferential diffusion, indicating that the preferential diffusive-thermal instability induced by preferential diffusion has a significant impact on the flame structure and can attenuate the effect of intrinsic hydrodynamic instability associated with buoyancy and velocity shear. Accordingly, the local mixing intensity is intensified by the strong turbulent strain in the unity Lewis number case, which leads to a higher value of scalar dissipation rate. In addition, the small Lewis numbers of major species H_2 and H affect the energy transfer due to the strong mass diffusion, and consequently the flame considering preferential diffusion exhibits higher temperature values than those predicted for the unity Lewis number case.

Apart from the instantaneous results of preferential diffusion, the statistical data of turbulent scalar transport show that the ranges of calculated and modelled scalar fluxes in the case considering preferential diffusion are clearly widened, while narrow distributions are formed in the unity Lewis number case. This suggests that the turbulent scalar flux is affected by preferential diffusion, which is attributed to the presence of the highly diffusive H_2 as well as the highly diffusive radical H. Moreover, there is an interesting observation that CGD of both the conserved and non-conserved scalars can be detected for both the unity Lewis number case and for the case considering preferential diffusion, especially in the interface region between the burnt gas and unburnt fresh fuel. The counter-gradient transport is closely related to the pressure-driven convective behavior due to the heat release in the interface region between the burnt products and unburnt hydrogen, which is subject to the pressure variation across the turbulent flame. Similar to that for premixed flames, the classical gradient model for the scalar closure may not work well for nonpremixed hydrogen flames.

References

[1] Jacobson MZ. Control of fossil-fuel particulate black carbon and organic matter, possibly the most effective method of slowing global warming. J Geophys Res 2002; 107: 1-22.

[2] Mason EA, Kronstadt B. Graham's Laws of Diffusion and Effusion J Chem Educ 1967; 44: 740-4.

[3] Katta VR, Goss LP, Roquemore WM. Numerical investigations of transitional H_2/N_2 jet diffusion flames. AIAA J 1994; 32: 84-94.

[4] Katta VR, Roquemore WM. On the structure of a stretched/compressed laminar flamelet-Influence of preferential diffusion. Combust Flame 1995; 100: 61-70.

[5] Jaberi FA, Miller RS, Mashayek F, Givi P. Differential diffusion in binary scalar mixing and reaction. Combust Flame 1997; 109: 561-77.

[6] Pitsch H, Peters N. A consistent flamelet formulation for non-premixed combustion considering differential diffusion effects. Combust Flame 1998; 114:26-40.

[7] Nilsen V, Kosály G. Differential diffusion in turbulent reacting flows. Combust Flame 1999; 117: 493-513.

[8] Takagi T, Yoshikawa Y, Yoshida K, Komiyama M, Kinoshita, S. Studies on strained non-premixed flames affected by flame curvature and preferential diffusion. Proc Combust Inst 1996; 26: 1103-10.

[9] Barlow RS, Dunn MJ, Sweeney MS, Hochgreb S. Effects of preferential transport in turbulent bluff-body-stabilized lean premixed CH_4/air flames. Combust Flame 2012; 159: 2563-75.

[10] Dunn MJ, Barlow RS. Effects of preferential transport and strain in bluff body stabilized lean and rich premixed CH_4/air flames. Proc Combust Inst 2013; 34: 1411-9.

[11] Hilbert R, Thévenin D. Influence of differential diffusion on maximum flame temperature in turbulent nonpremixed hydrogen/air flames. Combust Flame 2004; 138:

175-87.

[12] Im HG, Chen JH. Preferential diffusion effects on the burning rate of interacting turbulent premixed hydrogen-air flames. Combust Flame 2002; 131: 246-58.

[13] Smith LL, Dibble RW, Talbot L, Barlow RS, Carter CD. Laser Raman scattering measurements of differential molecular diffusion in turbulent nonpremixed jet flames of H_2/CO_2 fuel. Combust Flame 1995; 100: 153-60.

[14] Fu J, Tang C, Jin W, Huang Z. Effect of preferential diffusion and flame stretch on flame structure and laminar burning velocity of syngas Bunsen flame using OH-PLIF. Int J Hydrogen Energy 2014; 39: 12187-93.

[15] Ranga Dinesh KKJ, Jiang X, van Oijen JA. Hydrogen-enriched non-premixed jet flames: Compositional structures with near-wall effects. Int J Hydrogen Energy 2013; 38: 5150-64.

[16] Lipatnikov AN, Chomiak J. Molecular transport effects on turbulent flame propagation and structure. Prog Energy Combust Sci 2005; 31: 1-73.

[17] Pitsch H. Unsteady flamelet modeling of differential diffusion in turbulent jet diffusion flames. Combust Flame 2000; 123: 358-74.

[18] Richardson ES, Chen JH. Application of PDF mixing models to premixed flames with differential diffusion. Combust Flame 2012; 159: 2398-414.

[19] Park J, Lee DH, Yoon SH, Vu TM, Yun JH, Keel SI. Effects of Lewis number and preferential diffusion on flame characteristics in 80%H_2/20%CO syngas counterflow diffusion flames diluted with He and Ar. Int J Hydrogen Energy 2009; 34: 1578-84.

[20] Sutherland JC, Smith PJ, Chen JH. Quantification of differential diffusion in nonpremixed systems. Combust Theor Model 2005; 9: 365-83.

[21] Bisetti F, Chen JY, Chen JH, Hawkes ER. Differential diffusion effects during the ignition of a thermally stratified premixed hydrogen–air mixture subject to turbulence. Proc Combust Inst 2009; 32: 1465-72.

[22] Libby PA, Bray KNC. Countergradient diffusion in premixed turbulent flames. AIAA J 1981; 19: 205-13.

[23] Bray KNC, Libby PA, Masuya G, Moss JB. Turbulence production in premixed turbulent flames. Combust Sci Tech 1981; 25: 127–40.

[24] Jonathan HF, Peter AMK, Robert WB. Measurements of conditional velocities in turbulent premixed flames by simultaneous OH PLIF and PIV. Combust Flame 1999; 116: 220-32.

[25] Pfadler S, Leipertz A, Dinkelacker F, Wasle J, Winkler A, Sattelmayer T. Two-dimensional direct measurement of the turbulent flux in turbulent premixed swirl flames. Proc Combust Inst 2007; 31: 1337-44.

[26] Veynante D, Trouve A, E, Bray KNC, Mantel T. Gradient and counter-gradient scalar transport in turbulent premixed flames J Fluid Mech 1997; 332: 263-93.

[27] Veynante D, Poinsot T. Effects of pressure gradients on turbulent premixed flame. J Fluid Mech 1997; 353: 83-114.

[28] Luo KH. On local countergradient diffusion in turbulent diffusion flames. Proc Combust Inst 2000; 28: 489-95.

[29] Pfadler S, Kerl J, Beyrau F, Leipertz A, Sadiki A, Scheuerlein J, Dinkelacker F. Direct evaluation of the subgrid scale scalar flux in turbulent premixed flames with conditioned dual-plane stereo PIV. Proc Combust Inst 2009; 32: 1723-30.

[30] Chakraborty N, Cant RS. Effects of Lewis number on scalar transport in turbulent premixed flames. Phys Fluids 2009; 21: 035110.

[31] Tullis S, Cant RS. Scalar transport modeling in large eddy simulation of turbulent premixed flames. Proc Combust Inst 2002; 29: 2097-104.

[32] Bray KNC. Turbulent flows with premixed reactants. Turbulent reacting flows. Springer Berlin Heidelberg, 1980; 115-83.

[33] Veynante D, Vervisch L. Turbulent combustion modeling. Prog Energy Combust Sci

2002; 28: 193-266.

[34] Zimont VL, Biagioli F. Gradient, counter-gradient transport and their transition in turbulent premixed flame. Combust Theory Modelling 2002; 6: 79-101.

[35] Robin V, Mura A, Champion M. Direct and indirect thermal expansion effects in turbulent premixed flames. J. Fluid Mech 2011; 689: 149-82.

[36] Dong LL, Cheung CS, Leung CW. Characterization of impingement region from an impinging inverse diffusion flame jet. Int. J. Heat Mass Transfer 2013; 56: 360-9.

[37] Luo KH, Bray KNC. Combustion-induced pressure effects in supersonic diffusion flames. Twenty-Seventh Symposium (International) on Combustion/The Combustion Institute, 1998; 2165–71.

[38] Caldeira-Pires A, Heitor MV. Characteristics of turbulent heat transport in nonpremixed jet flames. Combust Flame 2001; 124: 213-24.

[39] Serra S, Robin V, Mura A, Champion M. Density variations effects in turbulent diffusion flames: modeling of unresolved fluxes. Combust Sci Technol 2014; 186: 1370-91.

[40] Ranga Dinesh KKJ, Jiang X, van Oijen JA. Numerical simulation of hydrogen impinging jet flame using flamelet generated manifold reduction. Int J Hydrogen Energy 2012; 37: 4502-15.

[41] van Oijen JA, de Goey LPH. Modelling of premixed laminar flames using flamelet-generated manifolds. Combust Sci Technol 2000; 161: 113-37.

[42] de Swart JAM, Bastiaans RJM, van Oijen JA, de Goey LPH, Stewart Cant R. Inclusion of preferential diffusion in simulations of premixed combustion of hydrogen/methane mixtures with flamelet generated manifolds. Flow Turbulence Combust 2010; 85: 473-511.

[43] Lele SK. Compact finite difference schemes with spectral-like resolution. J Comput Phys 1992; 103: 16-42.

[44] Williamson JH. Low-storage runge-kutta schemes. J Comput Phys 1980; 35: 48-56.

[45] Poinsot TJ, Lele SK. Boundary conditions for direct simulations of compressible viscous flows. J Comput Phys 1992; 101: 104-29.

[46] Thompson KW. Time dependent boundary conditions for hyperbolic systems. J Comput Phys 1987; 68: 1-24.

[47] Jiang X, Avital EJ, Luo KH. Sound generation by vortex pairing in subsonic axisymmetric jets. AIAA J 2004; 42: 241-8.

[48] Huerre P, Monkewitz PA. Absolute and convective instabilities in free shear layers. J Fluid Mech 1985; 159: 151-68.

[49] Ranga Dinesh KKJ, Jiang X, van Oijen JA, Bastiaans RJM, de Goey LPH. Hydrogen-enriched nonpremixed jet flames: effects of preferential diffusion. Int J Hydrogen Energy 2013; 38: 4848-63.

[50] Ranganath B, Echekki T. Effects of preferential and differential diffusion on the mutual annihilation of two premixed hydrogen–air flames. Combust Theor Model 2005; 9: 659-72.

[51] Liu F, Bao X, Gu J, Chen R. Onset of cellular instabilities in spherically propagating hydrogen-air premixed laminar flames. Int J Hydrogen Energy 2012; 37: 11458-65.

[52] Swaminathan N, Bilger RW. Direct numerical simulation of turbulent nonpremixed hydrocarbon reaction zones using a two-step reduced mechanism. Combust Sci Technol 1997; 127: 167-96.

[53] Ashurst WT, Kerstein AR, Kerr RM, Gibson CH. Alignment of vorticity and scalar gradient with strain rate in simulated Navier–Stokes turbulence. Phys Fluids 1987; 30: 2343.

Figure Captions

Fig. 1 Geometry of the nonpremixed hydrogen-air jet flame configuration and boundary conditions applied in the simulations.

Fig. 2 Instantaneous distributions of mass fractions of O_2, H, OH, HO_2 for the unity Lewis number (a1, a2, a3, a4) and the preferential diffusion (b1, b2, b3, b4) cases at t = 16.

Fig. 3 Instantaneous distributions of velocity vector fields for the two cases with the unity Lewis number assumption (a1, a2, a3) and preferential diffusion (b1, b2, b3) at different time instants t = 16 (a1, b1), 20 (a2, b2), 24 (a3, b3).

Fig. 4 Scatterplots of mass fractions of O_2, H, OH, HO_2 for the unity Lewis number (a1, a2, a3, a4) and the preferential diffusion (b1, b2, b3, b4) cases at t = 16.

Fig. 5 Scatterplots of temperature fields (a1, b1) and scalar dissipation rates (a2, b2) for the two cases with the unity Lewis number assumption (a1, a2) and preferential diffusion (b1, b2) in the mixture fraction space at t = 16.

Fig. 6 Variations of non-conserved scalar flux $\widetilde{u''Y''}$ against the scalar gradient of Favre-averaging reaction progress variable $\partial\tilde{Y}/\partial x$. (a) The unity Lewis number case; (b) The case considering preferential diffusion.

Fig. 7 Variations of conserved scalar flux $\widetilde{u''Z''}$ against the scalar gradient of Favre-averaging mixture fraction $\partial\tilde{Z}/\partial x$. (a) The unity Lewis number case; (b) The case considering preferential diffusion.

Fig. 8 The streamwise profiles of turbulent scalar flux $\widetilde{u''Y''}$ and the scalar gradient of Favre-averaging reaction progress variable $\partial\tilde{Y}/\partial x$ at the centerline y = 6. (a) The unity Lewis number case; (b) The case considering preferential diffusion.

Fig. 9 The streamwise profiles of turbulent scalar flux $\widetilde{u''Y''}$ and the scalar gradient of Favre-averaging reaction progress variable $\partial\tilde{Y}/\partial x$ at the shear layer y = 5.5. (a) The unity Lewis number case; (b) The case considering preferential diffusion.

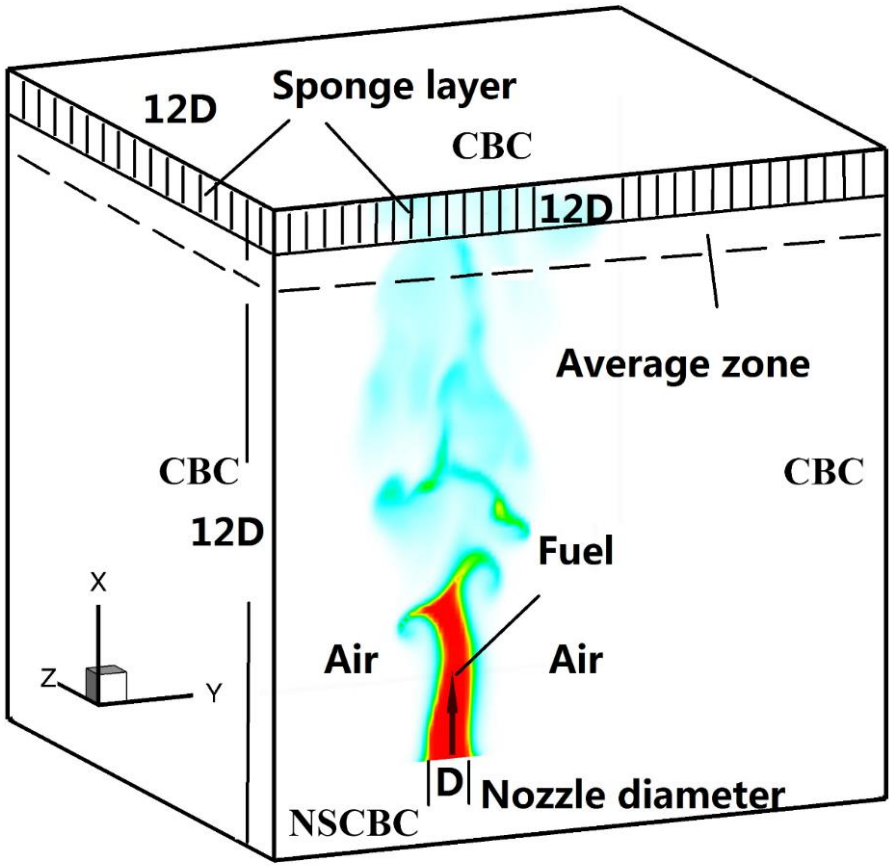

Fig. 1 Geometry of the nonpremixed hydrogen-air jet flame configuration and boundary conditions applied in the simulations.

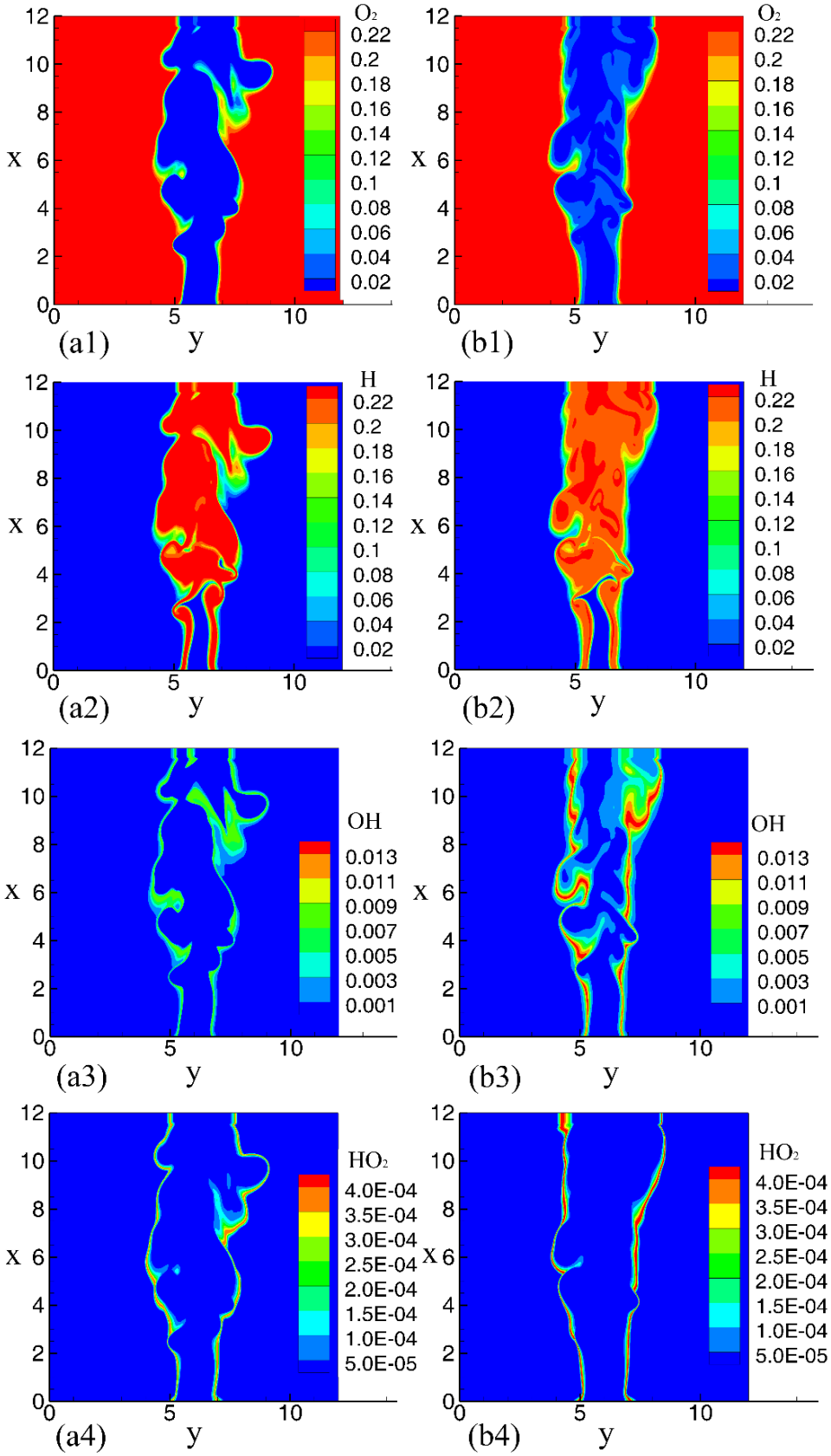

Fig. 2 Instantaneous distributions of mass fractions of O_2, H, OH, HO_2 for the unity Lewis number (a1, a2, a3, a4) and the preferential diffusion (b1, b2, b3, b4) cases at t = 16.

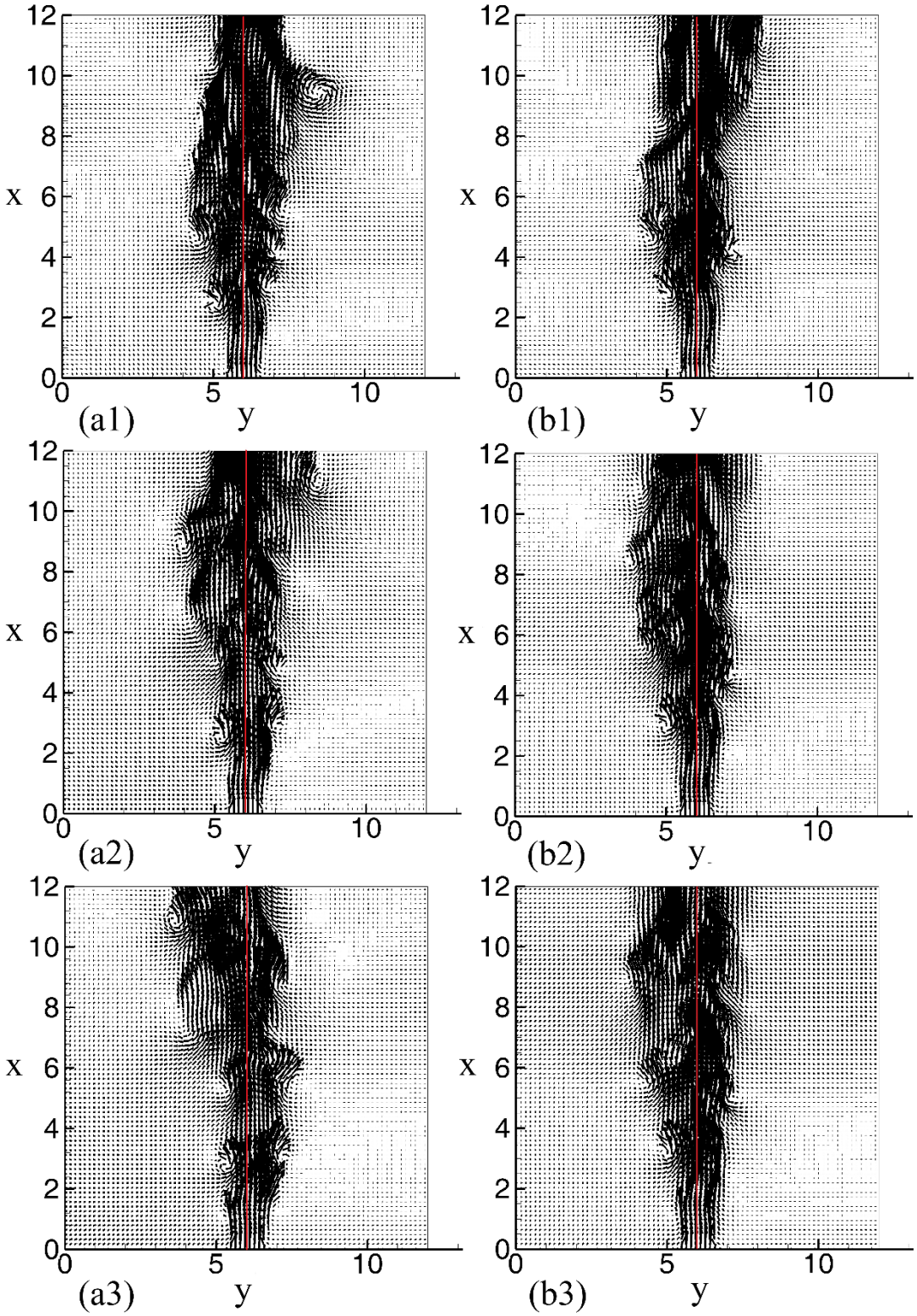

Fig. 3 Instantaneous distributions of velocity vector fields for the two cases with the unity Lewis number assumption (a1, a2, a3) and preferential diffusion (b1, b2, b3) at different time instants t = 16 (a1, b1), 20 (a2, b2), 24 (a3, b3).

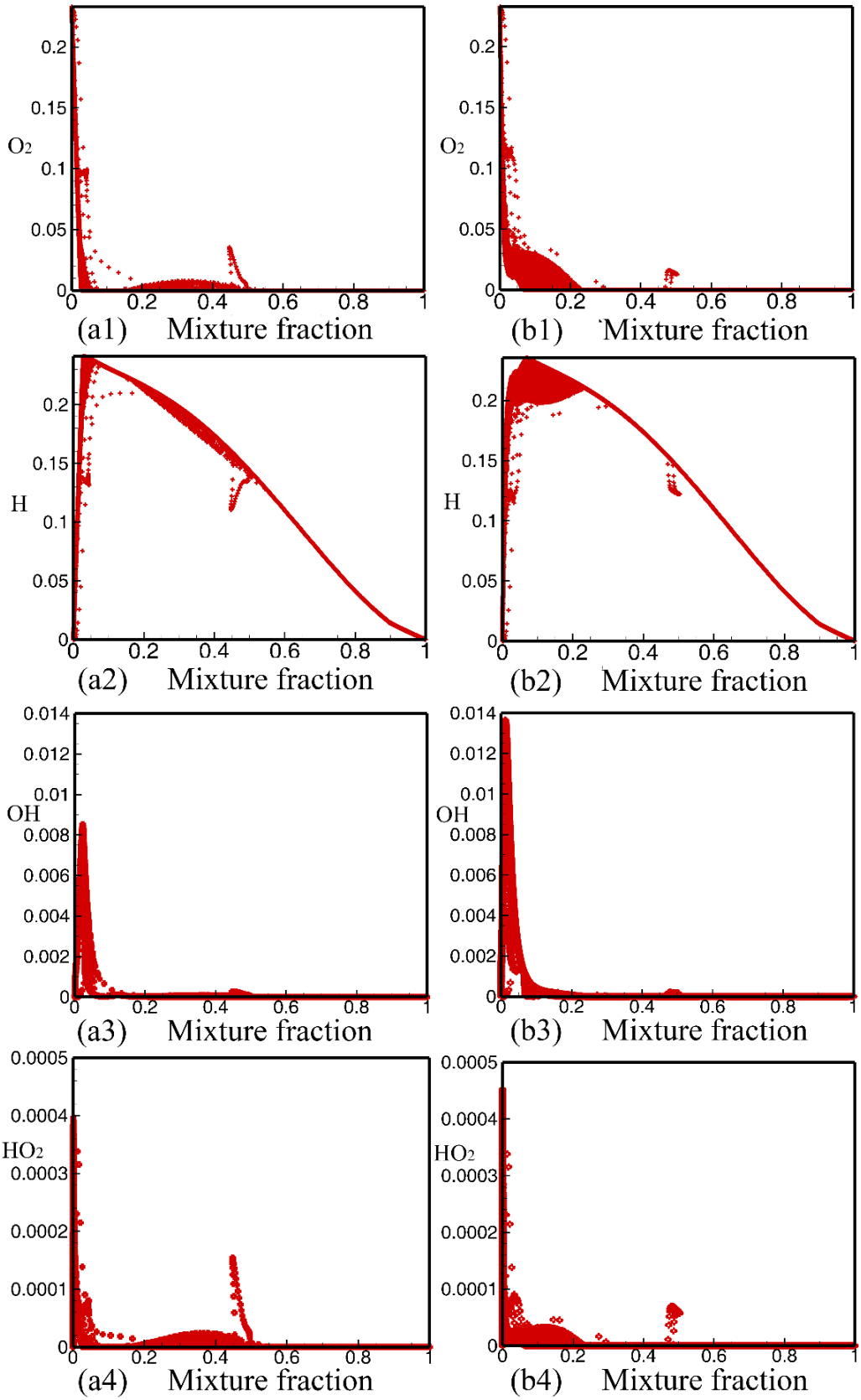

Fig. 4 Scatterplots of mass fractions of O_2, H, OH, HO_2 for the unity Lewis number (a1, a2, a3, a4) and the preferential diffusion (b1, b2, b3, b4) cases at t = 16.

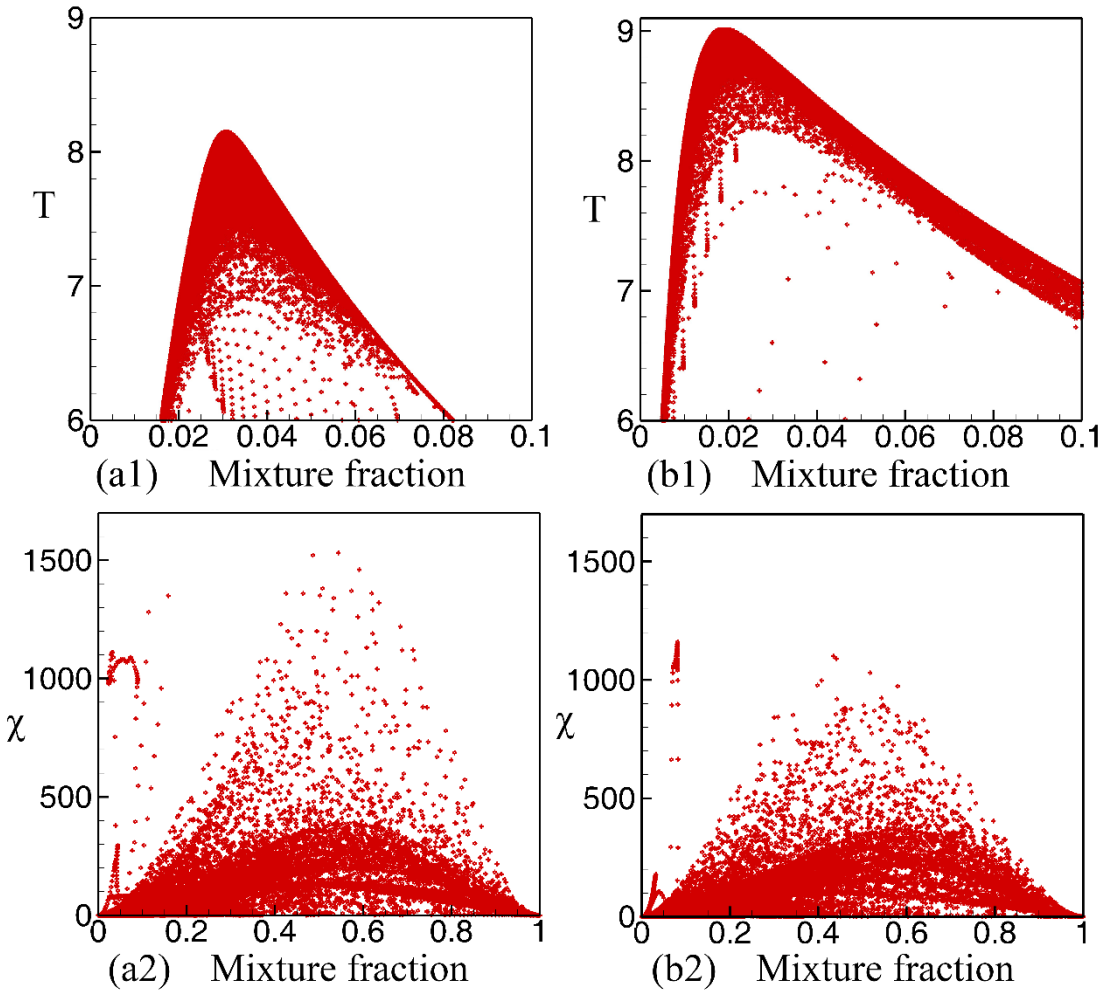

Fig. 5 Scatterplots of temperature fields (a1, b1) and scalar dissipation rates (a2, b2) for the two cases with the unity Lewis number assumption (a1, a2) and preferential diffusion (b1, b2) in the mixture fraction space at t = 16.

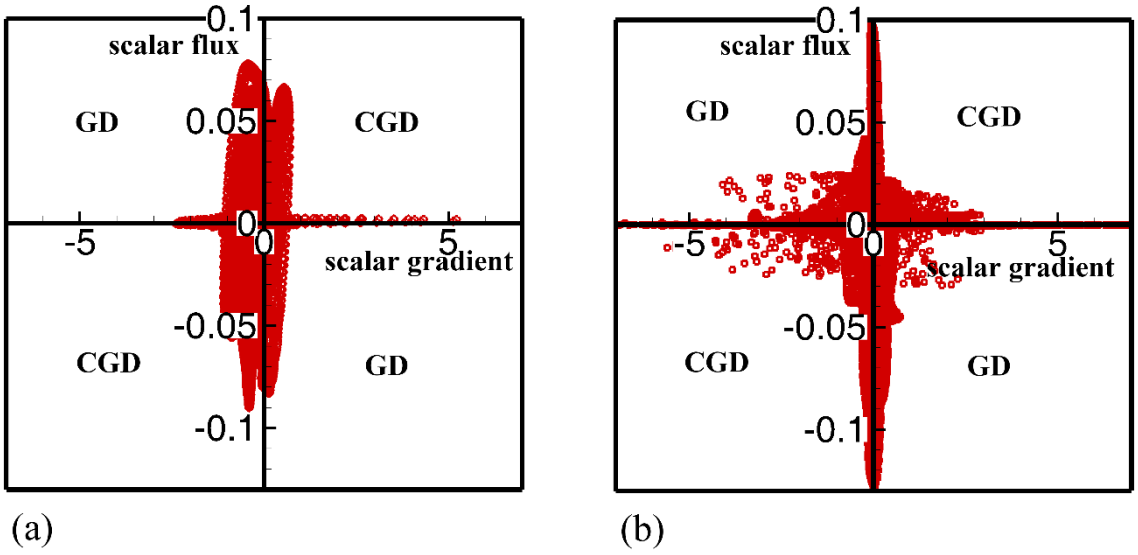

Fig. 6 Variations of non-conserved scalar flux $\widetilde{u''Y''}$ against the scalar gradient of Favre-averaging reaction progress variable $\partial\tilde{Y}/\partial x$. (a) The unity Lewis number case; (b) The case considering preferential diffusion.

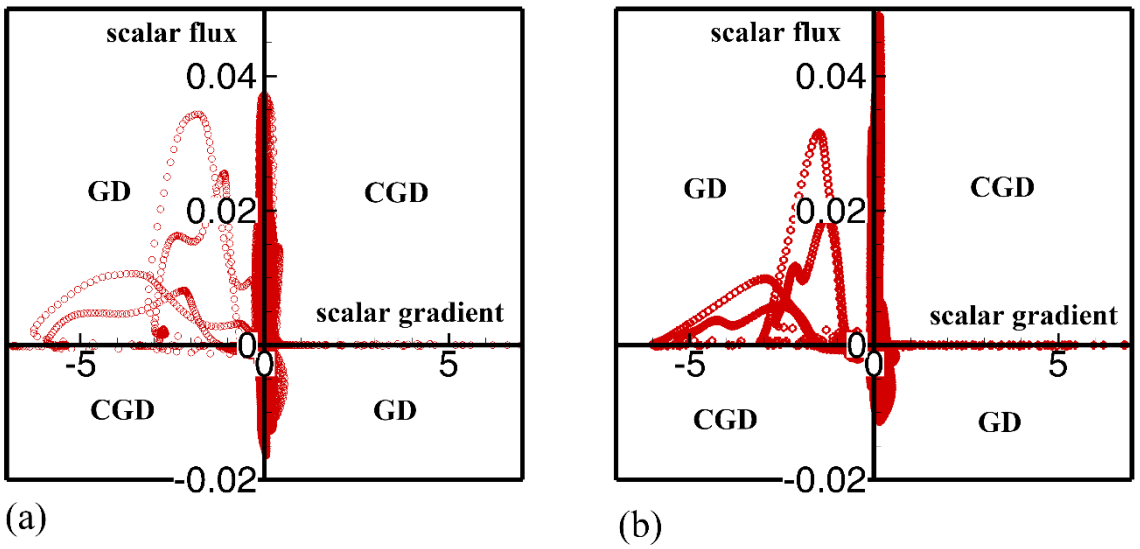

Fig. 7 Variations of conserved scalar flux $\widetilde{u''Z''}$ against the scalar gradient of Favre-averaging mixture fraction $\partial\tilde{Z}/\partial x$. (a) The unity Lewis number case; (b) The case considering preferential diffusion.

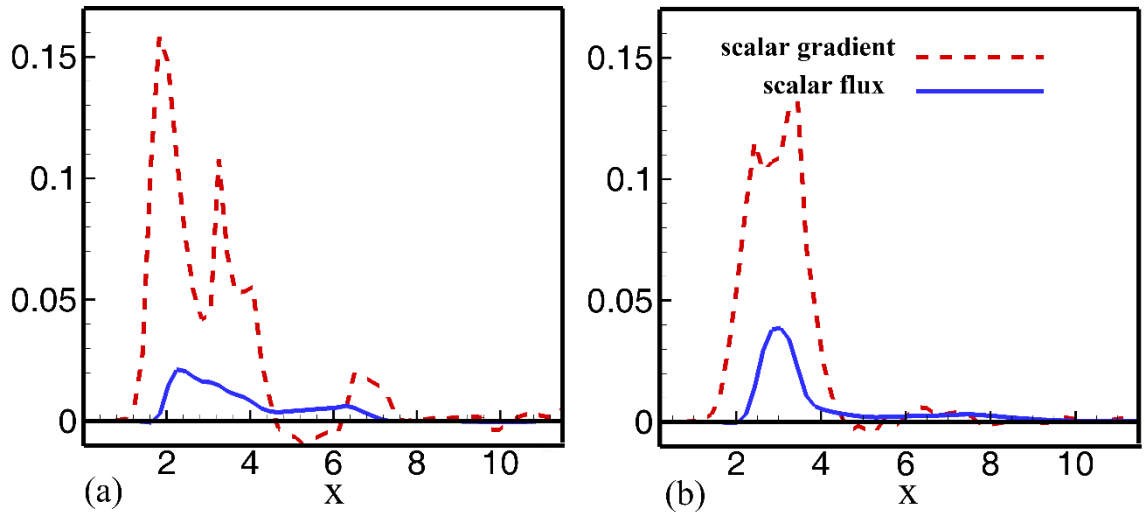

Fig. 8 The streamwise profiles of turbulent scalar flux $\widetilde{u''Y''}$ and the scalar gradient of Favre-averaging reaction progress variable $\partial\tilde{Y}/\partial x$ at the centerline y = 6. (a) The unity Lewis number case; (b) The case considering preferential diffusion.

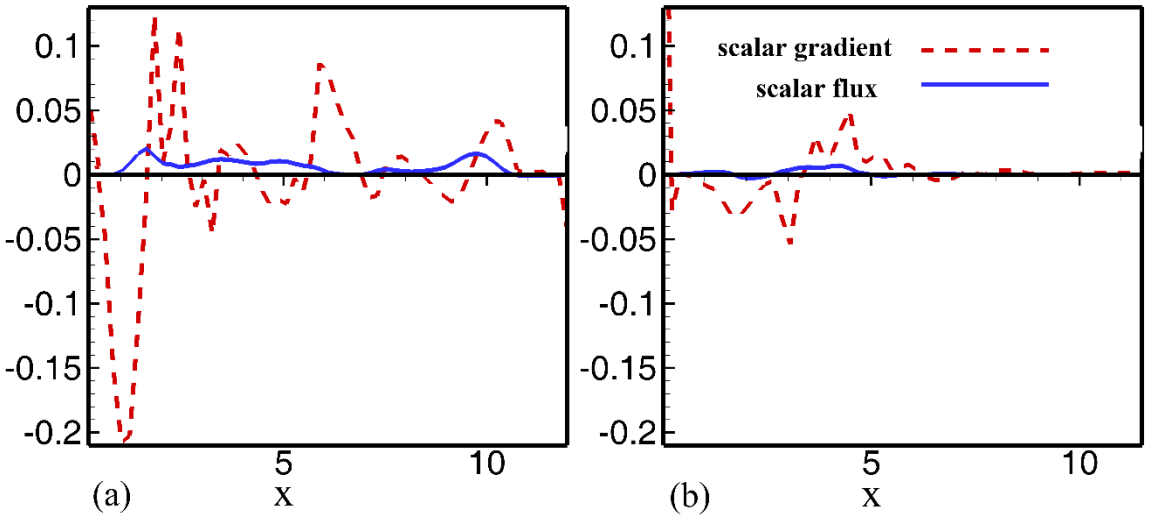

Fig. 9 The streamwise profiles of turbulent scalar flux $\widetilde{u''Y''}$ and the scalar gradient of Favre-averaging reaction progress variable $\partial\tilde{Y}/\partial x$ at the shear layer y = 5.5. (a) The unity Lewis number case; (b) The case considering preferential diffusion.